Electromagnetic imaging of separable obstacle problem

Xiuzhu Ye,* Rencheng Song, Krishna Agarwal, and Xudong Chen

Department of Electrical and Computer Engineering, National University of Singapore, 117576 Singapore
*yexiuzhu@nus.edu.sg

Abstract: The practical problem of imaging scatterers that are *separable* from the known obstacles is addressed. Using such *a priori* information, the obstacle is regarded as a known scatterer rather than part of the background and can be excluded from the retrieving process by reformulating the cost function. As a result, the proposed method transforms the problem into an inverse scattering problem with homogeneous background, and avoids the computationally intensive calculation of Green's function for inhomogeneous background (bases of the physical model of the problem). Meanwhile, the factors that influence the imaging quality for such kind of problem are also analyzed. Various difficult numerical examples are presented to show the good performance of our method. In addition, a data set of scattering experiments from the Institut Fresnel is tested to verify the validity of our method.

References and links

1. M. A. Fiddy and M. Testorf, "Inverse scattering method applied to the synthesis of strongly scattering structures," Opt. Express **14**(5), 2037–2046 (2006).
2. P. C. Chaumet, K. Belkebir, and R. Lencrerot, "Three-dimensional optical imaging in layered media," Opt. Express **14**(8), 3415–3426 (2006).
3. R. J. He, L. Y. Rao, S. Liu, W. L. Yan, P. A. Narayana, and H. Brauer, "The method of maximum mutual information for biomedical electromagnetic inverse problems," IEEE Trans. Magn. **36**(4), 1741–1744 (2000).
4. S. M. Ali, N. K. Nikolova, and M. H. Bakr, "Non-destructive testing and evaluation utilizing frequency-domain EM modeling," in Proceedings of the Second IASTED International Conference on Antennas, Radar, and Wave Propagation (Banff, CANADA, 2005), pp. 29–34.
5. S. Caorsi, A. Massa, and M. Pastorino, "A crack identification microwave procedure based on a genetic algorithm for nondestructive testing," IEEE Trans. Antenn. Propag. **49**(12), 1812–1820 (2001).
6. S. Caorsi, A. Massa, M. Pastorino, and M. Donelli, "Improved microwave imaging procedure for non-destructive evaluations of two-dimensional structures," IEEE Trans. Antenn. Propag. **52**(6), 1386–1397 (2004).
7. A. Massa, M. Pastorino, A. Rosani, and M. Benedetti, "A microwave imaging method for NDE/NDT based on the SMW technique for the electromagnetic field prediction," IEEE Trans. Instrum. Meas. **55**(1), 240–247 (2006).
8. M. Benedetti, M. Donelli, and A. Massa, "Multicrack detection in two-dimensional structures by means of GA-based strategies," IEEE Trans. Antenn. Propag. **55**(1), 205–215 (2007).
9. M. Dehmollaian, M. Thiel, and K. Sarabandi, "Through-the-wall imaging using differential SAR," IEEE Trans. Geosci. Rem. Sens. **47**(5), 1289–1296 (2009).
10. L. P. Song, C. Yu, and Q. H. Liu, "Through-wall imaging (TWI) by radar: 2D tomographic results and analyses," IEEE Trans. Geosci. Rem. Sens. **43**(12), 2793–2798 (2005).
11. A. J. Devaney and R. P. Porter, "Holography and the inverse source problem. Part II: Inhomogeneous media," J. Opt. Soc. Am. A **2**(11), 2006–2012 (1985).
12. J. M. Tualle, J. Prat, E. Tinet, and S. Avrillier, "Real-space Green's function calculation for the solution of the diffusion equation in stratified turbid media," J. Opt. Soc. Am. A **17**(11), 2046–2055 (2000).
13. S. He, L. Zhuang, F. Zhang, W. Hu, and G. Zhu, "Investigation of range profiles from buried 3-D object based on the EM simulation," Opt. Express **19**(13), 12291–12304 (2011).
14. S. Caorsi, A. Massa, M. Pastorino, M. Raffetto, and A. Randazzo, "Detection of buried inhomogeneous elliptic cylinders by a memetic algorithm," IEEE Trans. Antenn. Propag. **51**(10), 2878–2884 (2003).
15. X. Chen, "Subspace-based optimization method for inverse scattering problems with an inhomogeneous background medium," Inverse Probl. **26**(7), 074007 (2010).
16. A. Abubakar, W. Hu, P. M. van den Berg, and T. M. Habashy, "A finite-difference contrast source inversion method," Inverse Probl. **24**(6), 065004 (2008).

17. X. Ye, Y. Zhong, and X. Chen, "Reconstructing perfectly electric conductors by subspace-based optimization method with continuous variables," Inverse Probl. **27**(5), 055011 (2011).
18. A. Randazzo, G. Oliveri, A. Massa, and M. Pastorino, "Electromagnetic inversion with the multiscaling inexact Newton method-experimental validation," Microw. Opt. Technol. Lett. **53**(12), 2834–2838 (2011).
19. X. Ye, X. Chen, Y. Zhong, and K. Agarwal, "Subspace-based optimization method for reconstructing perfectly electric conductors," Prog. Electromagn. Res. **100**, 119–128 (2010).
20. S. Caorsi, M. Donelli, D. Franceschini, and A. Massa, "A new methodology based on an iterative multiscaling for microwave imaging," IEEE Trans. Microwave Theory Tech. **51**(4), 1162–1173 (2003).
21. M. Donelli, G. Franceschini, A. Martini, and A. Massa, "An integrated multiscaling strategy based on a particle swarm algorithm for inverse scattering problems," IEEE Trans. Geosci. Rem. Sens. **44**(2), 298–312 (2006).
22. M. Donelli, D. Franceschini, P. Rocca, and A. Massa, "Three-dimensional microwave imaging problems solved through an efficient multiscaling particle swarm optimization," IEEE Trans. Geosci. Rem. Sens. **47**(5), 1467–1481 (2009).
23. A. Y. Qing, "Electromagnetic inverse scattering of multiple perfectly conducting cylinders by differential evolution strategy with individuals in groups (GDES)," IEEE Trans. Antenn. Propag. **52**(5), 1223–1229 (2004).
24. P. Rocca, M. Benedetti, M. Donelli, D. Franceschini, and A. Massa, "Evolutionary optimization as applied to inverse scattering problems," Inverse Probl. **25**(12), 123003 (2009).
25. X. Chen, "Application of signal-subspace and optimization methods in reconstructing extended scatterers," J. Opt. Soc. Am. A **26**(4), 1022–1026 (2009).
26. J. Shen, X. Chen, Y. Zhong, and L. Ran, "Inverse scattering problem in presence of a conducting cylinder," Opt. Express **19**(11), 10698–10706 (2011).
27. J. M. Geffrin, P. Sabouroux, and C. Eyraud, "Free space experimental scattering database continuation: experimental set-up and measurement precision," Inverse Probl. **21**(6), S117–S130 (2005).
28. O. M. Bucci, N. Cardace, L. Crocco, and T. Isernia, "Degree of nonlinearity and a new solution procedure in scalar two-dimensional inverse scattering problems," J. Opt. Soc. Am. A **18**(8), 1832–1843 (2001).
29. M. D'Urso, T. Isernia, and A. F. Morabito, "On the Solution of 2-D Inverse Scattering Problems via Source-Type Integral Equations," IEEE Trans. Geosci. Rem. Sens. **48**(3), 1186–1198 (2010).
30. R. Autieri, M. D'Urso, T. Isernia, and V. Pascazio, "Inverse Profiling via an Effective Linearized Scattering Model and MRF Regularization," IEEE Trans. Geosci. Rem. Sens. **8**(6), 1021–1025 (2011).
31. T. Cui, Y. Qin, Y. Ye, J. Wu, G. Wang, and W. Chew, "Efficient low-frequency inversion of 3-D buried objects with large contrasts," IEEE Trans. Geosci. Rem. Sens. **44**(1), 3–9 (2006).
32. W. Chew and J. Lin, "A frequency-hopping approach for microwave imaging of large inhomogeineous bodies," IEEE Microw. Guid. Wave Lett. **5**(12), 439–441 (1995).
33. J. Ma, W. Chew, C. Lu, and J. Song, "Image reconstruction from TE scattering data using equation of strong permittivity fluctuation," IEEE Trans. Antenn. Propag. **48**(6), 860–867 (2000).
34. W. C. Chew, Waves and Fields in Inhomogeneous Media, Van Nostrand Reinhold, New York, 1990.
35. J. A. Kong, Electromagnetic Wave Theory (EMW. 2000).

1. Introduction

Inverse scattering problems are of great interest to scientists nowadays [1–33]. They have a wide application in the fields of optical diffraction tomography [2], bio-imaging [3], and non-destructive evaluation (NDE) [4–8]. One specific kind of inverse scattering problem is described as follows: 1) the problem involves imaging unknown scatterers hidden among known obstacles. 2) There is no overlap between the scatterers and obstacles. We refer to such kind of problem as separable obstacle problem (SOP).

The quality evaluation of the cores in optical fiber cable is a typical SOP. Another example is the evaluation of the dielectric slab waveguide, where its core layer can be seen as unknown scatterer and the outer cladding layers are the known obstacles. Some through wall imaging problems [9,10] such as detection of the furniture/humans in a room, inspecting the contents of closed parcels in standard shipment packages, and imaging the contents of storage tanks (made of dielectric walls), can also be classified as SOP. Thus, the study on SOP is of practical importance.

Traditionally, the SOP is treated as an inhomogeneous background inverse problem [11], because the obstacle is generally regarded as a part of the background medium. Thus, the Green's functions used for inhomogeneous background have complex forms [12]. Most of the published works consider only the cases where the (semi-)closed-form expressions of the corresponding Green's functions are available, such as half-space background medium [13,14] or infinite length layered medium [2,10]. However, when the obstacle is of arbitrary shape, numerical calculation of the Green's functions is needed. In [15], the finite element method (FEM) is adopted as the numerical method, while in [16] the finite difference (FD) approach is used to calculate the numerical Green's functions. However, the numerical

approximations of Green's functions introduce numerical errors into the discrete model and are quite computationally intensive.

A similar problem as SOP, the NDE of detecting cracks inside an object (called the host medium), has been studied in [5–8]. The free space Green's function was employed to build the scattering model in [5] where the object itself was considered as a scatterer but not the background, while [6–8] solved this NDE problem with inhomogeneous Green's function which took the object as inhomogeneous background. These papers optimized the crack parameters by genetic algorithms with assumption of rectangular cracks. The NDE problem studied in [5–8] is not a SOP because there is no prior separable (non-overlapping) information with the host.

In this paper, we aim to solve the SOP without recourse to the numerical calculation of Green's functions while still providing good reconstruction results. The main idea of the proposed approach is that the known obstacle can be treated as 'known scatterer' rather than part of the background. Therefore, the background is simply homogeneous and the elements corresponding to the obstacle can be excluded from the retrieving process of the unknowns by applying a mathematical reformulation to the cost function. The Green's function used has just the analytical form for the homogeneous background. For this reason, we refer to our scheme as SOP-homo. It's highlighted that the prior information of no overlap between the unknown scatterers and the known obstacles is essential for our method. Such specific condition is fulfilled very often in practice, like the examples presented above. For comparison, we refer to the methods that require numerical calculation of Green's function (such as FEM/FD related approaches) as the Obstacle Problem-inhomo (OP-inhomo), which is applicable to both separable and non-separable obstacles. Furthermore, if the *a priori* information of separable obstacle is also used in OP-inhomo, we call it Separable Obstacle Problem-inhomo (SOP-inhomo).

Because the inverse scattering problem is nonlinear and ill-posed, fictitious solution is obtained when the optimization traps into a local minimum. Therefore, it's necessary to discuss the optimization strategy used in the inversion. Generally, the optimization methods can be classified as two types, i.e., deterministic and stochastic. Deterministic methods include the inexact Newton method [18], the conjugate gradient method [15–17], steepest descent method [19], etc., which can deal with a large number of unknown parameters. However, the deterministic method usually has the risk of getting false solution if initial value is far from the true one. Stochastic methods such as the particle swarm optimization [21,22], genetic algorithm [5], and differential evolution [23] are seen as global optimization methods. However the unknowns are usually limited to a small number due to the computational amount. Therefore, each kind of optimization technique has its own merits and demerits [24]. In the present work, we use conjugate gradient method in optimization where a good initial value is obtained from both the subspace method and prior information of SOP.

We analyze various factors that influence the imaging quality of SOP, and finally give the strategy of choosing the more suitable modeling method for such problem. Various numerical results are given to validate SOP-homo and comparisons are also made with the other two methods mentioned above. Further, we provide a test of SOP-homo against the experimental data provided by Institut Fresnel (Marseille, France) to validate the efficiency of our method. Many numerical examples presented in this paper are much more complex and difficult than existing reported results so far. The numerical results indicate that the SOP-homo works well for SOP and has a better performance especially in the case of unknown scatterer adjacent to the obstacles.
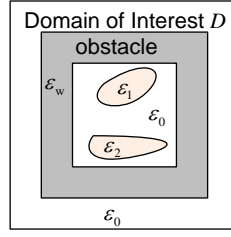
2. Forward problem

Fig. 1. A general scenario for separable obstacle problem (SOP).

The forward problem consists of determining the scattered field on receivers given the information of the scatterers and the incident field. In this section, we present the forward model, which is the foundation of the inverse problem. We consider a two-dimensional problem under transverse magnetic (TM) wave illumination. All the electric fields and currents are in the longitudinal z direction only. However, the theory can be directly extended to transverse electric or three-dimensional setups. The setup of the problem is depicted in Fig. 1. Inside the domain of interest D, the obstacle of relative permittivity ε_w surrounds the unknown scatterers. The wave number in obstacle is denoted as k_w. The physical properties of the obstacle are known *a priori*. N_{inc} cylindrical waves symmetrically illuminate the domain of interest. Then the scattered field is received by N_r antennas evenly distributed on a circle outside the domain of interest D, the positions of which are $\mathbf{r}_q$, $q = 1, 2, \ldots, N_r$. Thus, there are totally $N_r \times N_{inc}$ data points of measurements recorded in the scattered field matrix. We discretize the domain of interest into N square-shaped subunits, and the centers of subunits are located at $\mathbf{r}_1, \mathbf{r}_2, \ldots, \mathbf{r}_N$. Out of these N subunits, the number of subunits that belong to the known obstacle is N_w.

The scattered field and the incident field at $\mathbf{r}$ satisfy the following Helmholtz equations [34],

$$\left\lfloor \nabla^2 + k_b^2(\mathbf{r}) \right\rfloor E_z^{sca}(\mathbf{r}) = -[k^2(\mathbf{r}) - k_b^2(\mathbf{r})]E_z^{tot}(\mathbf{r}), \tag{1}$$

$$\left\lfloor \nabla^2 + k_b^2(\mathbf{r}) \right\rfloor E_z^{inc}(\mathbf{r}) = -S(\mathbf{r}), \tag{2}$$

where $k_b(\mathbf{r})$ denotes the background wave number and $k(\mathbf{r})$ is the wave number at point $\mathbf{r}$, $E_z^{tot} = E_z^{sca} + E_z^{inc}$ indicates the total electric field. The primary source is given by $S(\mathbf{r})$.

The integral solutions of Eq. (1) and Eq. (2) are

$$E_z^{sca}(\mathbf{r}) = \int_D g(k_b; \mathbf{r}, \mathbf{r}') \left\lfloor k^2(\mathbf{r}') - k_b^2(\mathbf{r}') \right\rfloor E_z^{tot}(\mathbf{r}')d\mathbf{r}', \tag{3}$$

$$E_z^{inc}(\mathbf{r}) = \int_D g(k_b; \mathbf{r}, \mathbf{r}')S(\mathbf{r}')d\mathbf{r}'. \tag{4}$$

Equation (3) can be rewritten into discrete form, and the total electric field on the mth subunit satisfies the self-consistent equation,

$$E_z^{tot}(\mathbf{r}_m) = E_z^{inc}(\mathbf{r}_m) + \sum_{i \neq m} ik_b \eta_b g(k_b; \mathbf{r}_m, \mathbf{r}_i) \xi_i E_z^{tot}(\mathbf{r}_m), \quad m = 1, 2, \ldots, N. \tag{5}$$

The scattering strength is given by,

$$\xi_i = -i\left(k_b / \eta_b\right)A_i \left\lfloor \varepsilon_r(\mathbf{r}_i) - 1 \right\rfloor, \tag{6}$$

where $\varepsilon_r(\mathbf{r}_i)$ and A_i denote the relative permittivity with respect to the background medium and the area of the ith subunit, respectively. $\eta_b = \sqrt{\mu_0/\varepsilon_b}$ is the impedance of the background medium, where μ_0 is the permeability of free space, and ε_b is the permittivity of the background medium. Then we can write the scattered field on the receivers in a matrix form, which we call the field equation,

$$\bar{E}^{\text{sca}} = \bar{\bar{G}}_{\text{S}} \cdot \bar{I}^{\text{d}}. \tag{7}$$

Here $\bar{\bar{G}}_{\text{S}}(q,m) = i k_b \eta_b g(k_b;\mathbf{r}_q,\mathbf{r}_m)$ for $m = 1,2,\ldots,N$ and $q = 1,2,\ldots,N_r$. Further, $\bar{I}^{\text{d}} = [I_z^{\text{d}}(\mathbf{r}_1), I_z^{\text{d}}(\mathbf{r}_2),\ldots,I_z^{\text{d}}(\mathbf{r}_N)]^{\text{T}}$, $\bar{E}^{\text{sca}} = [E_z^{\text{sca}}(\mathbf{r}_1), E_z^{\text{sca}}(\mathbf{r}_2),\ldots,E_z^{\text{sca}}(\mathbf{r}_{N_r})]^{\text{T}}$. The scattering strength ξ_i relates the total electric field to the induced current/contrast source by $I_z^{\text{d}}(\mathbf{r}_i) = \xi_i E_z^{\text{tot}}(\mathbf{r}_i)$. We get the state equation in a compact form,

$$\bar{I}^{\text{d}} = \bar{\bar{\xi}}(\bar{E}^{\text{inc}} + \bar{\bar{G}}_{\text{D}} \cdot \bar{I}^{\text{d}}), \tag{8}$$

where $\bar{\bar{G}}_{\text{D}}(m,i) = (i k_b \eta_b) g(k_b;\mathbf{r}_m,\mathbf{r}_i)$ and $\bar{E}^{\text{inc}} = [E_z^{\text{inc}}(\mathbf{r}_1), E_z^{\text{inc}}(\mathbf{r}_2),\ldots,E_z^{\text{inc}}(\mathbf{r}_N)]^{\text{T}}$. $\bar{\bar{\xi}}$ is a diagonal matrix composed by ξ_i, $i = 1,2,\ldots,N$.

$\bar{\bar{G}}_{\text{S}}$ and $\bar{\bar{G}}_{\text{D}}$ in the field equation Eq. (7) and state equation Eq. (8) are matrices of Green's functions, which map the induced current to the scattered field at the points outside and inside the investigation domain, respectively. According to the different definitions of the background medium, two kinds of forward models can be extracted from Eq. (1) to (8):

Model I: If the obstacle is regarded as part of the background, the background medium is inhomogeneous. The Green's function needs to be calculated by numerical methods such as FEM/FD etc.

Model II: If the obstacle is regarded as the known scatterer rather than the background, the background medium is homogeneous and is simply the free space. The Green's function exists analytically [35].

According to Eqs. (3) and (4), the calculated $\bar{E}^{\text{inc}}$ and $\bar{E}^{\text{sca}}$ are totally different in these two models. Comparisons between the two models are made as shown in Table 1.

In summary, by avoiding the numerical calculation of the Green's function, the advantages of model II over model I are:

Table 1. Comparison of the Model I and Model II

	k_b	$\bar{\bar{G}}_{\text{D}} \& \bar{\bar{G}}_{\text{S}}$	$\bar{E}^{\text{inc}}$	$\bar{E}^{\text{sca}}$
Model I	$k_b(\mathbf{r}) = \begin{cases} k_w, \mathbf{r} \in \text{obstacle} \\ k_0, \mathbf{r} \in \text{air} \end{cases}$	Numerical–inexact and computationally intensive	Numerical – numerical noise contained	Numerical – numerical noise contained
Model II	k_0	Analytical – exact and easy to compute	Analytical – no numerical noise	Analytical – no numerical noise

i. The computation complexity is reduced,
ii. The computing time is reduced,
iii. The numerical noise to the inverse model is avoided.

The OP/SOP-inhomo employs the model I while the SOP-homo uses model II. Some references mentioned in our paper can also be classified into these two models. The method in [5] has taken model II by regarding both the crack and object as scatterers, while [6–8] has taken model I by regarding the object under detection as the inhomogeneous background. Further, the $\bar{E}^{\text{inc}}$ for model I (background incident field) is actually the electric field including both the original incident field and the scattered field from the obstacle. Although model I

introduces numerical errors into the discrete model due to the computation of Green's functions, it usually has a smaller degree of nonlinearity in inverse problem than model II, which will be discussed later in detail. On the other hand, if the prior information of separable obstacle is given, model II shall be able to utilize this information more efficiently.

3. Inverse problem

The inverse scattering problem is to retrieve the relative permittivity matrix $\bar{\bar{\xi}}$ from the measured scattered field. We use the subspace based optimization method (SOM) as a demonstration reconstruction method to show the detail of solving the SOP. Namely, we will do the reformulation on SOM (so as to get the so-called SOP-homo) in order to utilize the prior information of SOP.

3.1 Outline of standard SOM

The main idea of SOM is to firstly obtain the deterministic part of the induced current $\bar{I}^{\mathrm{s}}$ by using Eq. (6) in [25]. Then the remaining part of the induced current $\bar{I}^{\mathrm{n}} = \bar{I}^{\mathrm{d}} - \bar{I}^{\mathrm{s}}$ is obtained through optimization. The two terms $\bar{\bar{\xi}}$ and $\bar{I}^{\mathrm{n}}$ are alternatively updated using the conjugate gradient method. The action of fixing one portion of the induced current first can greatly speed up the optimization process.

The cost function is the sum of residues from both field and state equations,

$$f(\bar{\bar{\xi}}) = \sum_{p=1}^{N_{\mathrm{inc}}} \left(\Delta_p^{\mathrm{fie}} \Big/ \left\| \bar{E}_p^{\mathrm{sca}} \right\|^2 + \Delta_p^{\mathrm{sta}} \Big/ \left\| \bar{I}_p^{\mathrm{s}} \right\|^2 \right),$$ (9)

where $\|\cdot\|$ is the Euclidean length of a vector.

The Δ^{fie} denotes the residue in the field equation and is given by

$$\Delta^{\mathrm{fie}} = \left\| \bar{E}^{\mathrm{sca}} - \bar{\bar{G}}_{\mathrm{s}} \cdot \bar{I}^{\mathrm{d}} \right\|^2.$$ (10)

The residue in the state equation is defined to be,

$$\Delta^{\mathrm{sta}} = \left\| \bar{I}^{\mathrm{d}} - \bar{\bar{\xi}}(\bar{E}^{\mathrm{inc}} + \bar{\bar{G}}_D \cdot \bar{I}^{\mathrm{d}}) \right\|^2.$$ (11)

The algorithm is briefly presented below and we refer the readers to [15,17] for the details. Here $\bar{I}_{p,n}^{\mathrm{n}}$, $p = 1, 2, \ldots, N_{\mathrm{inc}}$ denotes the remaining part of induced current in the nth step of iteration. And $\bar{\bar{\xi}}_n$ denotes the matrix of scattering strength in the nth step of iteration.

Step 1: Data preparation

Step 2: Initialization: $n = 0$.

Step 3: Iteration: $n = n + 1$.

Step 3.1: Update $\bar{I}_{p,n}^{\mathrm{n}}$, while regarding $\bar{\bar{\xi}}_n$ as a known parameter.

Step 3.2: Update $\bar{\bar{\xi}}_n$, while regarding $\bar{I}_{p,n}^{\mathrm{n}}$ as a known parameter.

Step 4: If termination condition is satisfied, stop iteration. Otherwise, go to Step 3.

3.2 Reformulation of SOM for SOP

In this section we introduce how to reformulate the SOM so as to utilize the prior information of SOP. Since no scatterers overlap with the obstacles, the subunits belonging to the obstacles can be fixed throughout the whole updating process. Therefore the number of unknowns in

matrix $\bar{\bar{\xi}}$ is actually $N - N_{\mathrm{w}}$ which is the number of non-obstacle elements. Thus in step 1 and 2 of the updating algorithm, the initial guess of $\bar{\bar{\xi}}$ is modified according to the prior information of the obstacle.

In step 3.2, since $\bar{I}_{p,n}^{\mathrm{n}}$ is regarded as a known parameter, the field residue as in Eq. (10) is fixed and only state residue changes as a consequence of updating $\bar{\bar{\xi}}_n$. In Eq. (9), the cost function can be written as summation of each individual element as,

$$f\left(\bar{\bar{\xi}}\right) = \sum_{p=1}^{N_{\mathrm{inc}}} \left(\frac{\Delta_p^{\mathrm{fie}}}{\left\| \bar{E}_p^{\mathrm{sca}} \right\|^2} + \frac{\sum_{i=1}^{N} \left(\Delta_p^{\mathrm{sta}} \right)_i}{\left\| \bar{I}_p^{\mathrm{s}} \right\|^2} \right).$$ (12)

Thus, we can split the objective function into three parts: the field residue $\left(\Delta_{p,n}^{\mathrm{fie}} \right)$, the state residue corresponding to the obstacle subunits $\left(\Delta_{p,n}^{\mathrm{sta}} \right)^{\mathrm{obs}}$ and the state residue corresponding to the non- obstacle subunits $\left(\Delta_{p,n}^{\mathrm{sta}} \right)^{\mathrm{non\text{-}obs}}$, i.e.,

$$f\left[\left(\bar{\bar{\xi}}_n \right)_i \right] = \frac{1}{2} \sum_{p=1}^{N_{\mathrm{inc}}} \left(\frac{\Delta_{p,n}^{\mathrm{fie}}}{\left\| \bar{E}_p^{\mathrm{sca}} \right\|^2} + \sum_{i=1}^{N_{\mathrm{w}}} \frac{\left(\Delta_{p,n}^{\mathrm{sta}} \right)_i^{\mathrm{obs}}}{\left\| \bar{I}_p^{\mathrm{s}} \right\|^2} + \sum_{i=1}^{N-N_{\mathrm{w}}} \frac{\left(\Delta_{p,n}^{\mathrm{sta}} \right)_i^{\mathrm{non\text{-}obs}}}{\left\| \bar{I}_p^{\mathrm{s}} \right\|^2} \right).$$ (13)

On the right hand side of Eq. (13), the first two terms are constant with respect to the unknowns (the $(\bar{\bar{\xi}}_n)_i$ on non-obstacle subunits). Thus, only the last term in Eq. (13) contributes in the CG update with respect to the unknowns $(\bar{\bar{\xi}}_n)_i$, $i = 1, 2, \ldots, N - N_{\mathrm{w}}$. The details of updating $\bar{\bar{\xi}}_n$ are similar to [15] and are omitted here. This optimization scheme has the advantage that the number of unknowns is significantly reduced compared to the general SOM model, which results in a faster convergence speed.

3.3. Discussion about nonlinearity

Although there are various advantages for the SOP-homo scheme, it is important to note that a trade-off is also involved. Even though we have excluded the obstacle from the updating process of unknowns, the currents in the known obstacle and the unknown scatterers, coexist in our scheme. On the other hand, in OP/SOP-inhomo, the known obstacle is regarded as belonging to the background and the induced currents correspond to only the contrast of unknown scatterer with respect to the inhomogeneous background. This is because the multiple scattering effects between the scatterers and obstacles have already been accounted for in the inhomogeneous background Green's function. As a consequence, the SOP-homo has a higher nonlinearity compared to OP/SOP-inhomo, which may reduce the quality of reconstruction, for example in the cases where the known obstacle has a higher permittivity than the unknown scatterer. In our numerical examples, we shall use the degree of nonlinearity proposed in [28], which is defined by $\left\| \bar{\bar{\xi}} \cdot \bar{\bar{G}}_{\mathrm{D}} \right\|_2$ in source type model, to indicate the nonlinearity of the problem. The degree of nonlinearity is a useful tool for quantifying the nonlinearity and has been used by several works on inverse scattering problem [29,30].

In summary, there are two factors that influence the quality of reconstruction in SOP. The first factor is the Green's functions and related numerical inaccuracies. The second factor is the nonlinearity of the model used for the problem. SOP-homo performs better in the first factor while OP/SOP-inhomo usually perform better in the second factor. Also, if the problem

is SOP, the proposed scheme can also be used in the differential formulations in the form of SOP-inhomo. Then, the benefits of both the differential formulation and the less number of unknowns can be derived.

In the application of optical fiber or waveguide evaluation, the unknown scatterers (core) usually have a higher permittivity than the obstacle (cladding), such that SOP-homo is a good choice for this kind of problem. On the other hand, for complicated problems (like the through wall imaging problems presented in Section 1) where nonlinearity is quite high, it is better to use the inhomogeneous Green's function to model the problem and then adopt the SOP-inhomo.

In addition, the problem of local minima will be stronger for the case of high contrast scatterers. The multi-scaling method proposed in [20] can reduce the risk of local minima. However the deterministic optimization schemes still have the risk of getting the solution trapped into the local minima. Thus the stochastic optimization is mandatory for such case. One possible solution is the method proposed by [21,22], which integrate the multi-scaling strategy with the stochastic optimizer. Thus the problem of local minima can be effectively avoided. Other possible approaches include the low frequency wave detection [31] and frequency hopping [32,33]. An agreed viewpoint on this issue is to utilize as much available information as possible in the inversion. The proposed SOP methodology is also developed under such track to incorporate the prior information into the optimization.

4. Numerical result

We present six numerical examples to validate our method. The first five numerical examples are comparisons between the OP/SOP-inhomo and SOP-homo, in order to examine the influencing factors on imaging quality. In the last example, one experimental example from the data set provided by Institut Fresnel (Marseille, France) [27] is used to validate the efficiency of the SOP-homo.

In the first five numerical examples, since SOM is used in SOP-homo as the optimization scheme, the FEM-SOM in [15] is taken as a comparison method. Depending on whether or not the *separable* obstacle information is applied, we denote the two editions of FEM-SOM as the OP-inhomo and SOP-inhomo, respectively.

The domain of interest for all the first five numerical examples is square of size $2\lambda \times 2\lambda$ and is discretized into $N = 45 \times 45$ square subunits. $N_{\text{inc}} = 10$ cylindrical waves are used as incident sources. The scattered field is measured by $N_{\text{r}} = 30$ receivers evenly distributed around a circle of radius 5λ. In all these five examples, the measurement data are got by method of moment and are contaminated by 10% white Gaussian noise. For all the three methods (SOP-homo, SOP/OP-inhomo), the optimization stops after 50 iterations. And for quantitative comparison, we define the average relative error

$$e = \frac{\sum_{i=1}^{N} \left| \varepsilon_{\text{r\_true},i} - \varepsilon_{\text{r\_rec},i} \right| \big/ \varepsilon_{\text{r\_true},i}}{N}, \tag{14}$$

where $\varepsilon_{\text{r\_true}}$ represents the true value of relative permittivity and $\varepsilon_{\text{r\_rec}}$ stands for the reconstructed value. For all the examples, the values of e are listed in Table 2. The units for the label of coordinates in figures are λ for the first five examples.
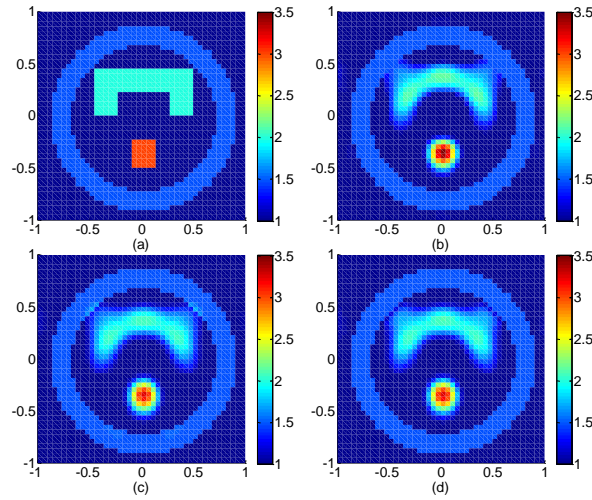
4.1 Example 1

Fig. 2. The configuration of scatterer in the first numerical example. The scattering data are contaminated with 10% white Gaussian noise. (a) Exact profile. (b) Reconstructed profile by SOP-homo. (c)Reconstructed profile by OP-inhomo. (d) Reconstructed profile by SOP-inhomo.

In this example, we aim to image one concave scatterer as well as one square scatter inside an annulus obstacle.

The outer radii and inner radii of the obstacle are 0.9λ and 0.7λ respectively. The relative permittivity of the obstacle is 1.5. There are two scatterers in the interior area of the obstacle. The first scatterer is an 'n' shaped scatterer with $\varepsilon_r = 2$ and the second scatterer is a square scatterer with $\varepsilon_r = 3$. The shapes and positions of these scatterers are shown in Fig. 2(a). Figure 2(b) ~(d) are the reconstruction results for SOP-homo, OP-inhomo and SOP-inhomo respectively. The reconstructed profiles in Fig. 2(b) ~(d) show that all methods clearly retrieve the positions and permittivities of the scatterers, including the concave area of the "n" shaped scatterer. The reconstruction errors presented in Table 2 show SOP-homo performs better than OP/SOP-inhomo. The reason of worse performance of SOP-inhomo than SOP-homo can be explained by its lower accuracy of Green's function.

4.2 Example 2

In the second example, we consider scatterers adjacent to the known obstacle. Such scatterers are difficult to reconstruct due to the proximity to the obstacle.

As shown in Fig. 3 (a), the known obstacle is square shaped, with the outer side length 1.63λ and the inner side length 1.26λ, and its relative permittivity is 1.5. There is an annular scatterer in the interior region of the obstacle, with inner and outer radii 0.25λ and 0.4λ, respectively, and its relative permittivity is 2. The centers of both the known square obstacle and the annular scatterer are at the origin. There are two small scatterers (similar to the presence of unanticipated clutters) adjacent to the known obstacle and in the corner, with the relative permittivities of 1.4 and 1.5 respectively.

Fig. 3 (b)~(d) are the reconstruction results for SOP-homo, OP-inhomo and SOP-inhomo respectively. We see that the position, the shape, as well as the relative permittivity of the annulus inside the obstacle are well reconstructed. Besides, the two objects adjacent to the obstacle are also seen clearly in Fig. 3 (b) and Fig. 3(d), while the square obstacle appears blurred by the adjacent objects in Fig. 3 (c). This is mainly because in OP-inhomo, the obstacle is regarded as background and the optimization updates the permittivity in the region of the obstacle as well. While in SOP-homo/SOP-inhomo the obstacle is regarded as known

scatterer and its permittivity is not allowed to change during the iteration. From Table 2 we see that the relative error of SOP-homo is still smaller than those of the other two.
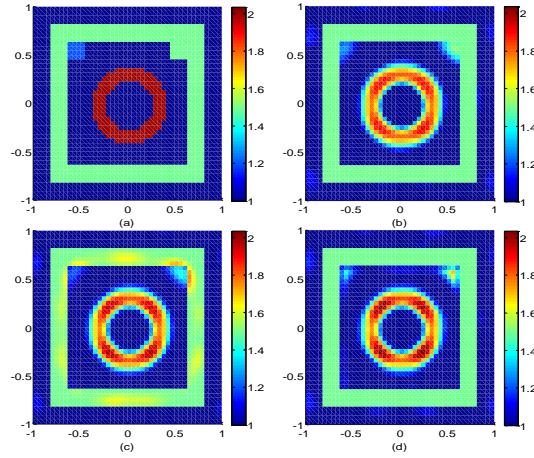

Fig. 3. The configuration of scatterer in the second numerical example. The scattering data are contaminated with 10% white Gaussian noise. (a) Exact profile. (b) Reconstructed profile by SOP-homo. (c)Reconstructed profile by OP-inhomo. (d) Reconstructed profile by SOP-inhomo.
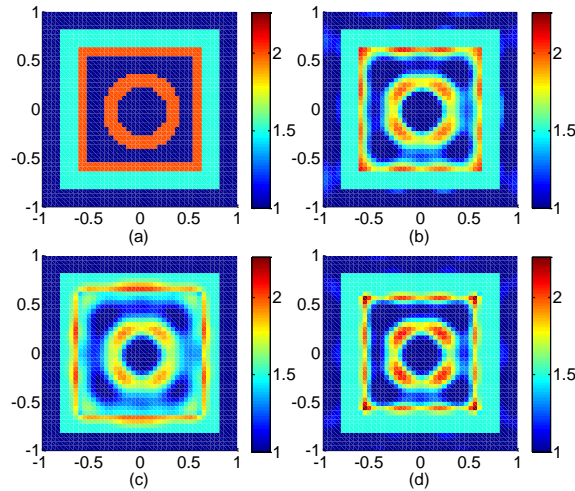

Fig. 4. The configuration of scatterer in the third numerical example. The scattering data are contaminated with 10% white Gaussian noise. (a) Exact profile. (b) Reconstructed profile by SOP-homo. (c)Reconstructed profile by OP-inhomo. (d) Reconstructed profile by SOP-inhomo.

4.3 Example 3

The third example is more challenging. In this example the inner surface of the obstacle is coated with a thin layer of a material with relative permittivity 2. The physical properties of the annular object as well as the obstacle remain the same as in the second example and the thickness of inner layer is 0.07λ, see Fig. 4(a).

From the reconstructed pattern in Fig. 4(c) which is the obtained by OP-inhomo, we see that the both the obstacle and its inner layer appear blurred. While Fig. 4(b) and Fig. 4(d) for SOP-homo and SOP-inhomo are much better, which proves again that the usage of the prior

information of separable obstacle demonstrates better results in the cases where the object is placed near the obstacle.
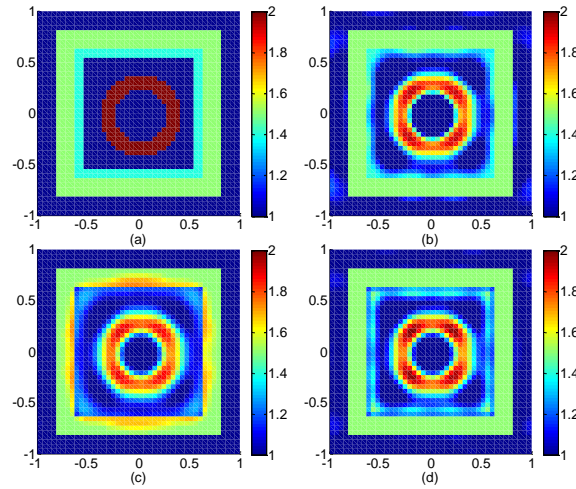
4.4 Example 4

Fig. 5. The configuration of scatterer in the fourth numerical example. The scattering data are contaminated with 10% white Gaussian noise. (a) Exact profile. (b) Reconstructed profile by SOP-homo. (c)Reconstructed profile by OP-inhomo. (d) Reconstructed profile by SOP-inhomo.

In the fourth example, the setup is the same as the third example except that the inner layer has a relative permittivity of 1.4, which is lower than the obstacle, as seen in Fig. 5(a).

From Fig. 5(b)~(d) and Table 2, it is clearly seen that SOP-homo and SOP-inhomo reconstruct the inner layer of the obstacle as well as the annulus better than the OP-inhomo.
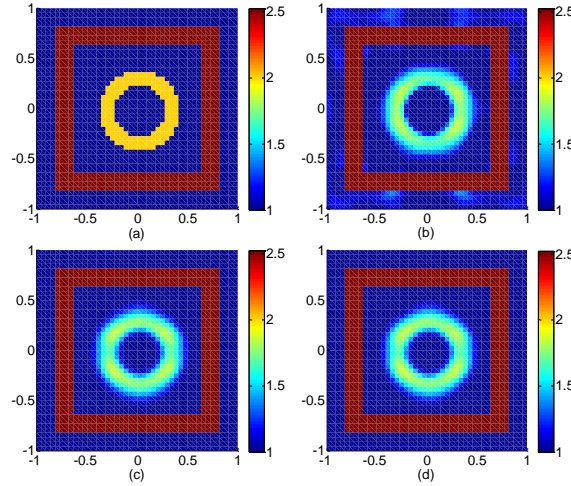

Fig. 6. The configuration of scatterer in the fifth numerical example. The scattering data are contaminated with 10% white Gaussian noise. (a) Exact profile. (b) Reconstructed profile by SOP-homo. (c) Reconstructed profile by OP-inhomo. (d) Reconstructed profile by SOP-inhomo.

4.5 Example 5

As indicated previously, the SOP-homo compromises in nonlinearity to avoid the computationally intensive Green's function calculation. This example highlights the aspect of nonlinearity. In this example the shape of the obstacle and the annulus object remain the same as the previous examples. The only difference is the relative permittivity of the obstacle is 2.5, higher than the unknown scatterer as seen in Fig. 6(a).

Table 2. Relative Errors in Reconstructions of Examples 1-5

	SOP-homo	OP-inhomo	SOP-inhomo
1st	0.0364	0.0432	0.0431
2nd	0.0337	0.0368	0.0355
3rd	0.0724	0.1125	0.0769
4th	0.0500	0.0698	0.0477
5th	0.0553	0.0423	0.0420

Comparing the results in Fig. 6(b) ~(d) and also from the errors in Table 2, we can see that SOP-homo gives a worse result than OP/SOP-inhomo in this example. This is mainly because the obstacle has a higher relative permittivity than the unknown scatterer, thus the induced current on the obstacle is stronger than that on the scatterer, which results in higher nonlinearity in SOP-homo compared to OP/SOP-inhomo (where the obstacle is treated as the background and no induced current appears on the obstacle).
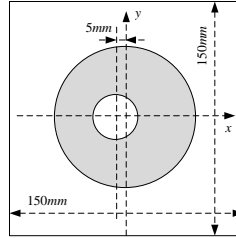

Fig. 7. Configuration of *FoamDielIntTM*

4.6 Example 6

At last, in order to verify the validity of SOP-homo against the experimental data, we adopt the experimental data set collected by Institut Fresnel (Marseille, France). The experiment is carried out in a two dimensional setting with TM and TE illuminations. The details of the experimental configuration can be found in [27]. Here in this paper the data set "*FoamDielIntTM*" is tested, which can be seen as a SOP if part of scatterers known *a priori*. The measured data are multi-frequency and we only use the single frequency data corresponding to 2GHz under the TM illumination.

$N_{inc} = 8$ incident waves evenly illuminate the domain around a circle of radius $R = 1.67\text{m}$. For each illumination, the scattered field is collected by 241 receiving locations no further than 60° to the transmitter with a distance of 1.67m from the origin. The configuration of the domain of interest is depicted as Fig. 7. The domain of interest is of the size $150 \times 150\text{mm}^2$. A foam cylinder of diameter 80mm and $\varepsilon_r = 1.45 \pm 0.15$ is centered at the origin. A plastic cylinder of diameter 31mm and $\varepsilon_r = 3 \pm 0.3$ is located inside the foam cylinder centered at $(-0.005, 0)$.

Firstly the foam cylinder is considered as the separable (known) obstacle and the plastic cylinder is the unknown scatterer. In the second test, we consider the plastic cylinder as the separable (known) obstacle while the foam cylinder as the unknown scatterer.

The inversion is done by the SOP-homo. For inversion, the domain of interest is discretized into a grid of 45×45 subunits. The unit of length in Fig. 8 is meter (m). From Fig. 8, we can see that both results are quite satisfactory by considering the *separable* information of the obstacle. The location and the relative permittivity of the unknown scatterers are both well reconstructed.
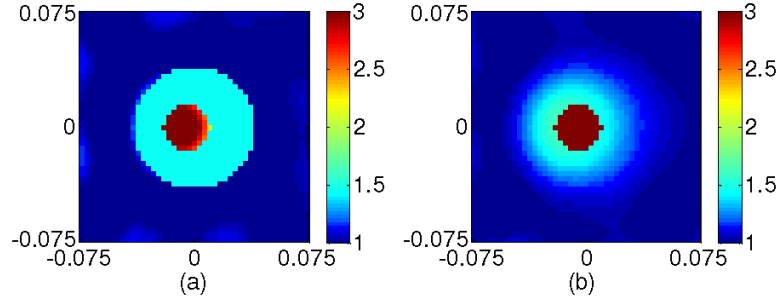

Fig. 8. Single-frequency reconstruction at 2GHz using SOP-homo for *FoamDielIntTM*. (a) the foam cylinder is the known obstacle (b) the plastic cylinder is the known obstacle

4.7 Further discussion about the results

Table 3. Degrees of Nonlinearity for Examples 1-5

	SOP-homo	SOP/OP-inhomo
1st	3.9531	3.9008
2nd	2.5529	2.4385
3rd	2.8552	2.5665
4th	2.5769	2.4538
5th	4.0690	2.6670

In order to verify our analysis about the nonlinearity for the SOP-homo and OP/SOP-inhomo, and also to quantitatively evaluate the nonlinearity for all the numerical examples, degree of nonlinearity [28], which is defined by $\left\| \bar{\bar{\xi}} \cdot \bar{\bar{G}}_{\mathrm{D}} \right\|_2$ in source type model, is calculated in our numerical simulations. Here the elements of matrix $\bar{\bar{\xi}}$ are given by Eq. (6), from which we can see the scattering strengths on the obstacle for OP/SOP-inhomo are zero values, while the scattering strengths on the obstacle in SOP-homo are non-zero values. Thus the degrees of nonlinearity for OP/SOP-inhomo are smaller than those in SOP-homo. In Table 3, we list the degrees of nonlinearity. We see the SOP-homo has a larger degree of nonlinearity than the other two methods in all five examples, and the degree contrast is especially sharp in the last example, which coincides with the discussion in section 3.3.

Obviously, SOP-inhomo performs better than OP-inhomo in all these examples because it takes use of the *separable obstacle* information and thus has fewer unknowns compared to the latter one. It is shown that the imaging resolution of SOP is improved greatly after the use of the prior separable information.

In summary, the first five numerical results verify the theoretical analysis in section 3.3. The last example has proved the validity of SOP-homo in solving the experimental data.

5. Conclusion

Our paper provides a comprehensive discussion on the imaging of SOP. We have introduced a new method called SOP-homo which utilizes the *a priori* information of certain known obstacles that are separable (do not overlap with) the unknown scatterers. The reconstruction performance of SOP is influenced by both the accuracy of the Green's function in the forward model and the nonlinearity of the inverse model. We conclude that: (1) SOP-homo runs much faster than SOP/OP-inhomo since the homogeneous background Green's function is applied.

(2) For the scatterers with lower contrast than the obstacles, SOP-homo outperforms SOP/OP-inhomo (due to the higher accuracy of Green's function), whereas for the higher contrast case, the SOP-homo is inferior to the SOP/OP-inhomo (due to the higher nonlinearity of the inverse model). (3) SOP-homo shows good performance for experimental examples as well (as demonstrated in section 4.6).

We also highlight two points. Firstly, although the accuracy of the numerical Green's function can be easily improved by reducing the grid step length, this will also increase the computational burden and the computing time severely. Also, the increased number of unknowns makes the inverse problem more ill-posed and difficult to solve. Thus, a balance between the two factors, accuracy of the Green's function and the nonlinearity of the inverse model, should be considered to choose a proper method for such kind of problems. Secondly, although the SOP-homo is introduced in the framework of SOM, other methods based on the field-state equation of the electric-field integral equation model can also be reformulated to solve such kind of problems as long as the cost function is constructed in a similar form.

Acknowledgments